Electronic Supplementary Material (ESI) for Nanoscale.
This journal is © The Royal Society of Chemistry 2016

Supplementary Information

Simultaneous Topographical, Electrical and Optical Microscopy of Optoelectronic Devices at the Nanoscale

Naresh Kumar[1]*, Alina Zoladek-Lemanczyk[1], Anne A. Y, Guilbert[2], Weitao Su[3], Sachetan M. Tuladhar[2], Thomas Kirchartz[2,4,5], Bob C. SchroedeS10, Iain McCulloch[6,7], Jenny Nelson[2], Debdulal Roy[1] and Fernando A. Castro[1]*

[1]National Physical Laboratory, Teddington, Middlesex, U.K. TW11 0LW, [2]Department of Physics, Imperial College London, London, U.K. SW7 2AZ , [3] Institute of Materials Physics, Hangzou Dianzi University, 310018 Hangzou, China, [4] IEK-5 Photovoltaik, Forschungzentrum Juelich 52425, Germany, [5]Faculty of Engineering and CENIDE, University of Duisburg-Essen, 9 Carl-Benz-Strasse 199, 47057 Duisburg, Germany, [6]Department of Chemistry, Imperial College London, London, U.K. SW7 2AZ, [7]SPERC, King Abdullah University of Science and Technology (KAUST), Thuwal, 23955-6900, Saudi Arabia. *E-mail: naresh.kumar@npl.co.uk; fernando.castro@npl.co.uk

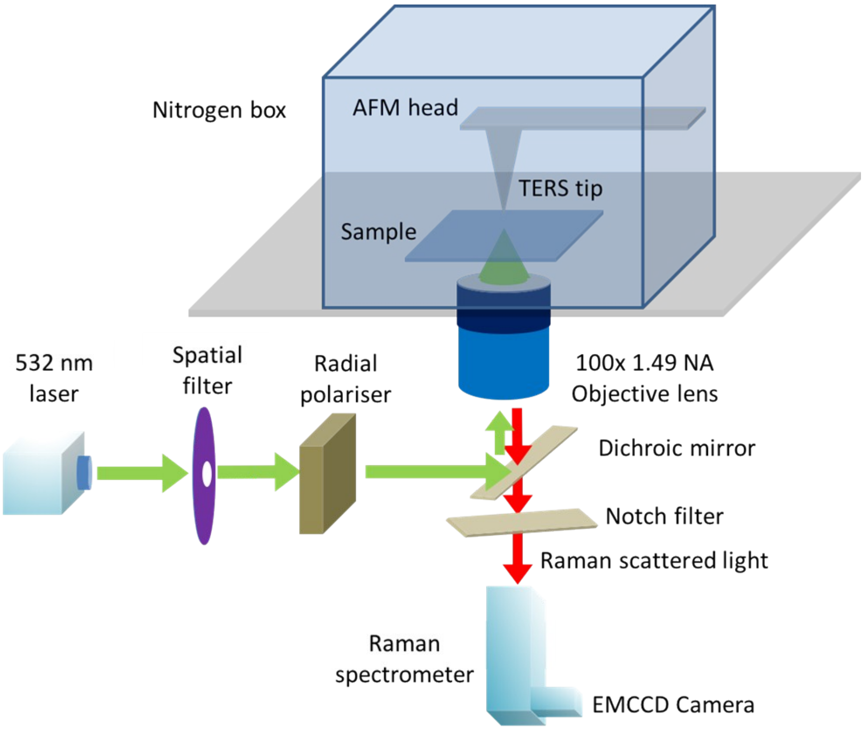

Fig. S1. Detailed schematic diagram of the optical set-up used in this work for simultaneous topographic, electrical and optical microscopy (STEOM) of operating organic solar cell devices.

Supplementary Note 1

Comparison of the macroscopic performance of C8SiIDT-BT:ICMA and C8SiIDT-BT:$PC_{61}BM$ blend solar cell devices

Device Structure: ITO/PEDOT:PSS/Blend/Ca/Al

Blend concentration in solution (prior to spin-coating):

- C8SiIDT-BT:ICMA = 20 mg/ml
- C8SiIDT-BT:$PC_{61}BM$ = 20 mg/ml

Thickness of the active layer: 66 – 70 nm

Area of the solar cells: 0.045 cm^2

Annealing conditions: 150 ^oC for 30 min

a) Effect of changing the fullerene derivative in the C8SiIDT-BT blends

Table S1: Macroscopic device performance of pristine C8SiIDT-BT:ICMA and C8SiIDT-BT:$PC_{61}BM$ blend solar cells with 1:1 relative blend ratio under 100 mW/cm^2 AM1.5G illumination.

Blends	**C8SiIDT-BT:ICMA (1:1)**	**C8SiIDT-BT:$PC_{61}BM$ (1:1)**
	Pristine	Pristine
J_{sc} (mA/cm^2)	2.79	6.34
V_{oc} (V)	0.93	0.91
FF	0.35	0.36
PCE %	0.91	2.08

J_{SC}: short circuit current density, **V_{OC}:** open circuit voltage, **FF:** fill factor, **PCE:** power conversion efficiency.

Pristine C8SiIDT-BT:ICMA (1:1) solar cell delivers a photocurrent of 2.8 mA/cm^2 and a PCE of 0.9%. Changing the fullerene derivative from ICMA to $PC_{61}BM$ results in more than twice improvement in the photocurrent and PCE in pristine C8SiIDT-BT:$PC_{61}BM$ (1:1) solar cell compared to the C8SiIDT-BT:ICMA (1:1) solar cell presumably due to a uniformly optimised morphology throughout the active layer. The increase in macroscopic photocurrent and PCE is well supported by the nanoscale STEOM measurements on pristine C8SiIDT-BT:$PC_{61}BM$ (1:1) solar cell device presented in the Supplementary Note 7.

b) Effect of increasing the fullerene content in C8SiIDT-BT:ICMA and C8SiIDT-BT:PC$_{61}$BM blends

Table S2: Macroscopic device performance of pristine C8SiIDT-BT:ICMA and C8SiIDT-BT:PC$_{61}$BM blend solar cells with 1:1 and 1:3 blend ratios under 100 mW/cm^2 AM1.5G illumination.

Blends	**C8SiIDT-BT:ICMA (1:1)**	**C8SiIDT-BT:ICMA (1:3)**	**C8SiIDT-BT:PC$_{61}$BM (1:1)**	**C8SiIDT-BT:PC$_{61}$BM (1:3)**
	Pristine	Pristine	Pristine	Pristine
J_{sc} (mA/cm^2)	2.79	3.51	6.34	6.05
V_{oc} (V)	0.93	0.92	0.91	0.89
FF	0.35	0.44	0.36	0.62
PCE %	0.91	1.42	2.08	3.34

Both C8SiIDT-BT:ICMA and C8SiIDT-BT:PC$_{61}$BM solar cells show an increase in PCE with the increase of fullerene ratio in the blends from 1:1 to 1:3. PCE for C8SiIDT-BT:ICMA solar cell increases from 0.91 % to 1.42 % whereas the PCE for C8SiIDT-BT:PC$_{61}$BM solar cell increases from 2.08 % to 3.34 %. The increase in the PCE (due to both J_{sc} and FF) with the increase of fullerene content in these macroscopic devices is consistent with the STEOM measurements of C8SiIDT-BT:ICMA blend solar cell at the nanoscale presented in Fig. 3, where an increase in photocurrent is observed from the regions of blend with a relatively higher fullerene content presumably due to nanoscale distribution of polymer molecules around larger fullerene aggregates that improve both charge dissociation at the polymer:fullerene interfaces as well as charge transport to the electrodes via larger fullerene aggregates.

c) Effect of annealing on the performance of C8SiIDT-BT:ICMA and C8SiIDT-BT:PC$_{61}$BM blends

Performance of both C8SiIDT-BT:ICMA and C8SiIDT-BT:PC$_{61}$BM blend solar cells is found to worsen after annealing. PCE decreases from 0.91 % to 0.58 % (photocurrent falls from 2.79 to 2.34 mA/cm^2) for the C8SiIDT-BT:ICMA solar cell, whereas it decreases from 2.08 % to 0.74 % (photocurrent falls by 50%, from 6.34 to 3.16 mA/cm^2) for the C8SiIDT-BT:PC$_{61}$BM blend cell solar cell. A similar worsening of C8SiIDT-BT:PC$_{61}$BM blend solar cell performance after annealing has been reported by Wang *et al.* (*Adv. Funct. Mater.* 2010, **20**, 492–499) This dramatic fall in the performance especially of C8SiIDT-BT:PC$_{61}$BM blend solar cell is explained by the nanoscale STEOM measurements of the annealed

Table S3: Macroscopic device performance of pristine and annealed C8SiIDT-BT:ICMA and C8SiIDT-BT:$PC_{61}BM$ blend solar cells with 1:1 blend ratio under 100 mW/cm^2 AM1.5G illumination.

Blends	**C8SiIDT-BT:ICMA (1:1)**		**C8SiIDT-BT:$PC_{61}BM$ (1:1)**	
	Pristine	Annealed	Pristine	Annealed
J_{sc} (mA/cm^2)	2.79	2.34	6.34	3.16
V_{oc} (V)	0.93	0.82	0.91	0.71
FF	0.35	0.30	0.36	0.33
PCE %	0.91	0.58	2.08	0.74

C8SiIDT-BT:$PC_{61}BM$ blend solar cell presented in Supplementary note 7, which reveal that the annealing leads to aggregation of fullerene molecules into relatively pure phase-separated domains that do not contain a nanoscale distribution of polymer molecule around them, unlike the fullerene domains of pristine C8SiIDT-BT:ICMA blend.

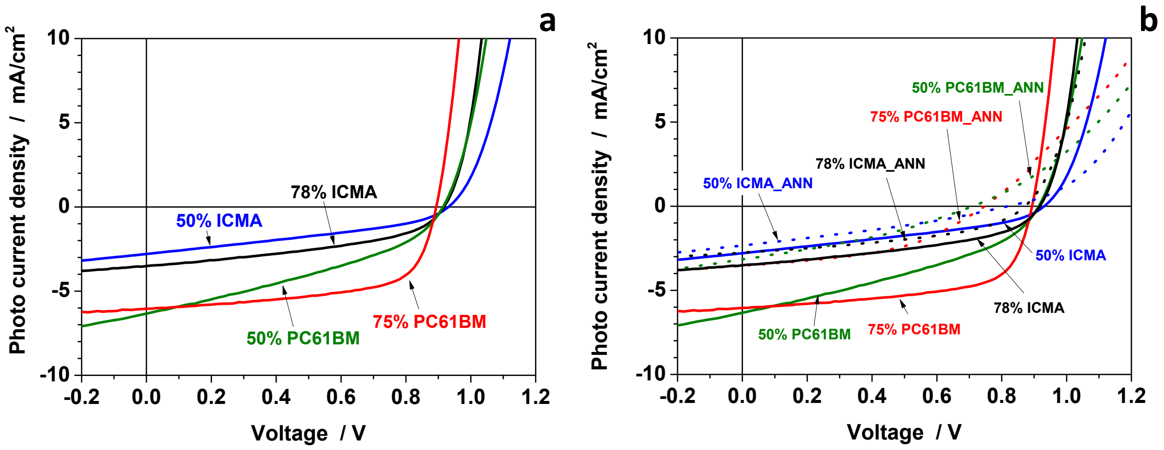

Fig. S2. Summary of current density – voltage characteristics of C8SiIDT-BT:ICMA and C8SiIDT-BT:$PC_{61}BM$ blend solar cells under 100 mW/cm^2 AM1.5G light with different blend ratios. (a) Effect of increasing the fullerene content on the photocurrent: Increasing fullerene content in the blend generally improves the photocurrent and PCE of both C8SiIDT-BT:ICMA and C8SiIDT-BT:$PC_{61}BM$ solar cells. (b) Effect of annealing on the photocurrent: A decrease in the photocurrent and PCE is observed upon thermal annealing (dotted lines) for both C8SiIDT-BT:ICMA and C8SiIDT-BT:$PC_{61}BM$ blends solar cells irrespective of the blend ratio.

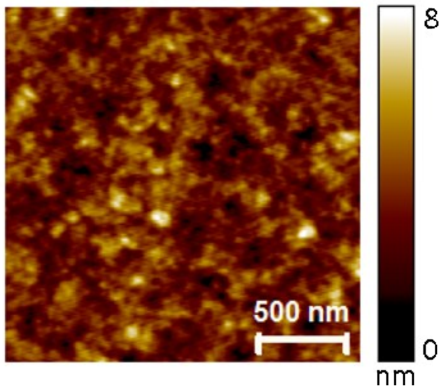

Fig. S3. Topography image of pristine C8SiIDT-BT:PC$_{61}$BM (1:1) blend measured using tapping-mode AFM. Compared to the topography of C8SiIDT-BT:ICMA blend shown in Fig 2b, topography of C8SiIDT-BT:PC$_{61}$BM blend shows absence of any large (submicron) scale features or phase-separated domains indicating a relatively thorough mixing of the polymer and fullerene molecules throughout the blend.

Supplementary Note 2

Plasmonic enhancement of optical (Raman and PL) signals on pristine C8SiIDT-BT and ICMA thin films

Enhancement factor (EF) of the near-field signal in a TEOS experiment is an estimate of the plasmonic enhancement of electromagnetic field at the tip-apex and hence could be used to measure of the performance of a TEOS tip. For a thin-film sample, the EF is usually calculated using the formula (Kumar et al. *Appl. Phys. Lett.* 2014, **104**, 123106):

$$EF = \frac{(I_{Tip-in} - I_{Tip-out}) / A_{NF}}{I_{Tip-out} / A_{FF}} \tag{1}$$

where I_{Tip-in} and $I_{Tip-out}$ are the optical signal intensities with the tip in contact and retracted from the sample, respectively. A_{FF} and A_{NF} are the areas of the thin-film contributing to the far-field and near-field optical signals, which can be estimated from the far-field and near-field spatial resolutions, respectively. For the TEOS system used in this work, the far-field spatial resolution has been experimentally measured from a line map across a single-wall carbon nanotube to be ≈ 225 nm.That implies that this confocal optical microscope cannot spatially resolve nanoscale features on the sample that are closer than 225 nm.

The near-field optical spatial resolution of our TEOS system is estimated from the TEPL map in Fig. 3b to be ≈ 19 nm. Fig. S4 shows the representative near-field optical spectra of pristine C8SiIDT-BT and ICMA thin films measured plasmonically active Ag-coated tip. About >90% of the Ag-coated tips prepared in our laboratory gave similar plasmonic enhancement. To calculate the EF, I_{Tip-in} and $I_{Tip-out}$ of the Raman and PL bands are calculated by fitting a set of Lorentzian (for Raman bands) and Gaussian (for PL bands) bands to the spectra. Using Eq. (1) the EFs of the 3800 cm^{-1} (667 nm) C8SiIDT-BT PL band, 5400 cm^{-1} (746 nm) ICMA PL band and 1382 cm^{-1} C8SiIDT-BT Raman band are calculated to be 263, 202 and 851, respectively.

It should be noted that this near-field enhancement of optical signals originates from the local plasmonic enhancement of electromagnetic field directly beneath the Ag-coated tip-apex, which has a diameter of ≈ 50 nm due to the localised plasmon (LSP) resonance of the metallic tip with the excitation laser. (Fig. 1). This nanoscale size of the near-field enables the nanoscale spatial resolution of optical maps obtained in this work.

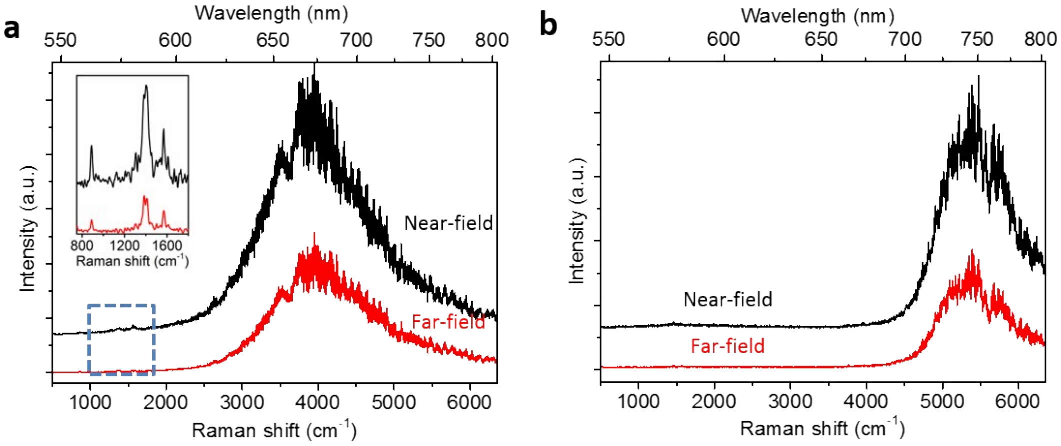

Fig. S4. (a) Near-field (Ag-coated tip in contact with the sample) and far-field (Tip retracted from the sample) optical spectra of pristine C8SiIDT-BT polymer thin film showing the plasmonic enhancement of Raman and PL signals at the tip-apex. Inset shows near-field (black) and far-field (red) spectra of the Raman bands of the polymer from the zoomed in area marked by the dotted square. (b) Near-field and far-field optical spectra of pristine ICMA thin film.

Supplementary Note 3

Spatial resolution of TEOS and photocurrent maps

Zoomed-in images of the fullerene TEPL map and photocurrent map shown in Fig. 3b and 3e are presented in Fig. S5a and S5c, respectively. The spatial resolution of a TEPL map is typically calculated from the full width at half maximum (FWHM) of a fitted Guassian curve to a line profile across a feature in the TEPL map. Using this procedure the spatial resolution of the TEPL map is estimated to be ≈ 19 nm as shown in Fig. S5b.

In tip-enhanced optical spectroscopy maps the intensity fluctuations due to random factors can sometimes introduce artefacts, which could be misinterpreted. To ensure this is not the case in our measurements, we present further analysis of the data to check if the intensity variations in the fullerene TEPL map shown in Fig. 3 and Supplementary Fig. S5a are indeed real.

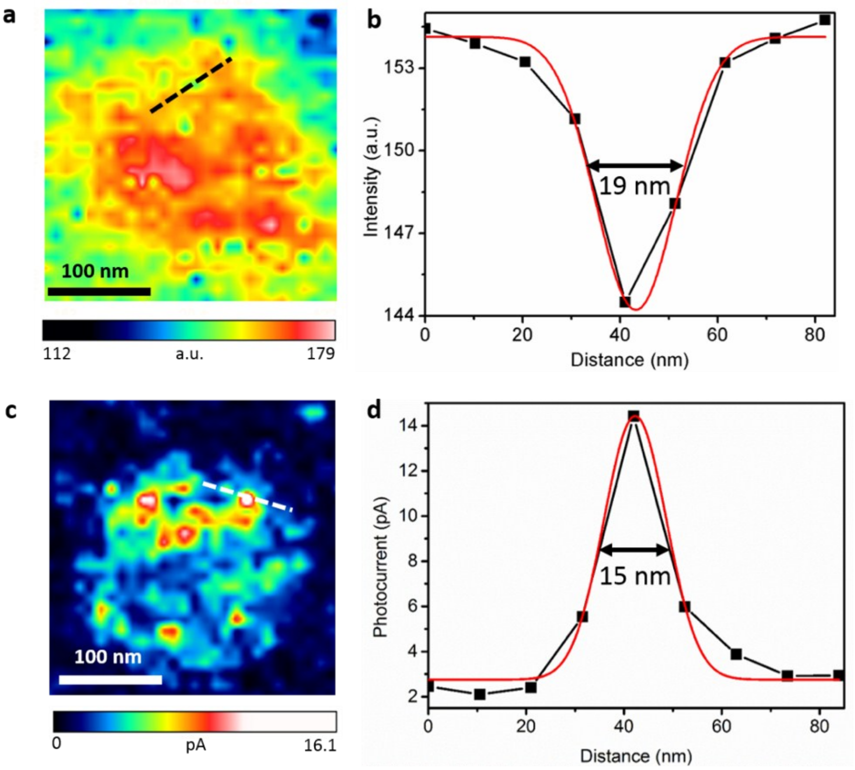

Fig. S5. (a) Zoomed-in image of the fullerene tip-enhanced PL (TEPL) map shown in Fig. 3b. (b) Intensity profile along the dashed line marked in a. FWHM of the Guassian fit to the intensity profile indicates that the spatial resolution of the TEPL map is ≈ 19 nm. (c) Zoomed-in image of the photocurrent map shown in Fig. 3e. (d) Intensity profile along the dashed while line marked in c. FWHM of the Guassian fit to the intensity profile indicates that the spatial resolution of the photocurrent map is ≈ 15 nm.

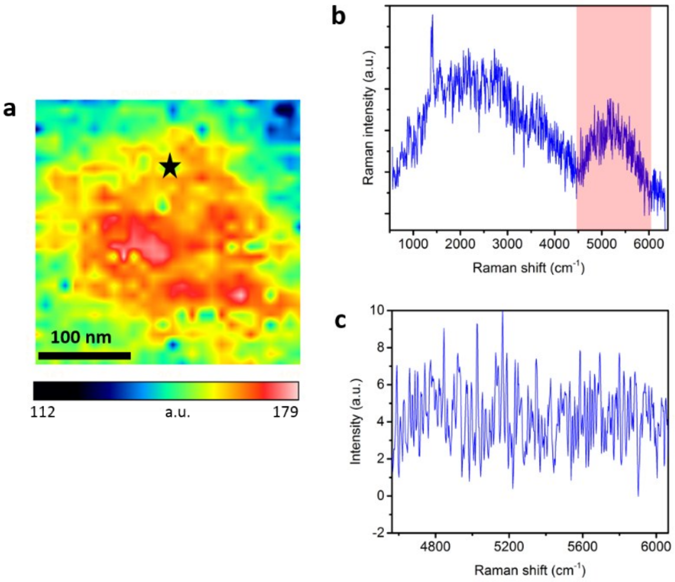

Fig. S6. (a) Zoomed-in image of the fullerene TEPL map shown in Fig. 3b. (b) TEPL spectrum measured at the location marked with a star in S6a. The fullerene PL region (4563 cm^{-1} – 6065 cm^{-1}) is highlighted in red. (c) Plot of the fullerene PL spectrum highlighted in S6b after subtracting a fitted Gaussian curve.

Fig. S6b shows the fullerene TEPL spectrum measured at the location marked with a star in the TEPL map shown in Fig. S6a. The fullerene PL region (4563 cm^{-1} – 6065 cm^{-1}) is highlighted in red in Fig. S6b. Fig. S6c shows a plot of the fullerene PL region highlighted in S6b after subtracting a fitted Gaussian curve to this spectral region. The noise level in the measured fullerene TEPL can be estimated from the standard deviation of the intensity shown in S6c.

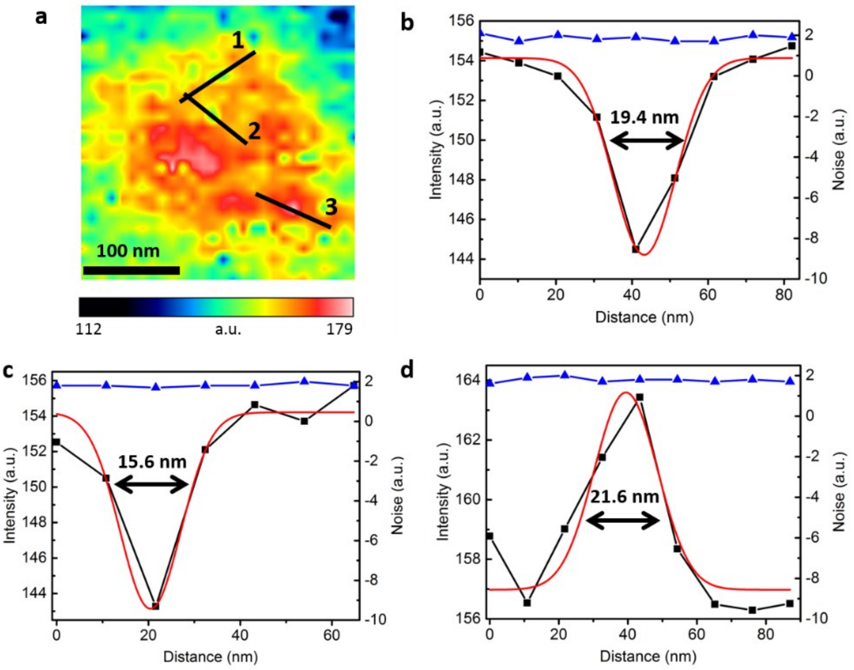

Fig. S7. (a) Zoomed-in image of the TEPL map shown in Fig. 3b of the manuscript. (b) Plot of the TEPL intensity (black squares) along line 1 marked in S7a. The noise level (blue triangles) calculated at each pixels along the line is also plotted for comparison. A Gaussian curve fitted to the intensity profile is shown in red. (c) Plots of TEPL intensity, noise level and Gaussian curve fitted to the intensity profile along line 2 marked in S7a. (d) Plots of TEPL intensity, noise level and Gaussian curve fitted to the intensity profile along line 3 marked in S7a.

Using the procedure outlined above, we have calculated the noise level in the TEPL spectra measured at individual pixels along the line marked as 1 in Figure S7a. The noise level (blue triangles) and the fullerene TEPL intensity (black squares) along the line are plotted in Fig S7b. It can be seen clearly that the difference in maximum and minimum PL intensity along the line is about 10 counts whereas the noise level remains fairly constant with an average value of 1.9 counts. This indicates that the intensity variation along the line are not due to random factors but arise from variation in the concentration of analyte molecules present underneath the tip-apex. A similar trend in the noise level and TEPL intensity is observed along the lines 2 and 3 marked in S7a as shown in Fig. S7c and S7d, respectively. Fig. S7b – d show the Gaussian curves (red colour) fitted to the intensity profiles along lines 1 – 3. The spatial resolution of the TEPL map estimated from the fitted Gaussian curves is < 20 nm.

The estimated spatial resolution of the fullerene TEPL map Fig. S7 is similar to the 20 nm spatial resolution of a TEPL map of a single-layer molybdenum disulphide (MoS_2) sample estimated following the same procedure, reported recently by our group using similar Ag-coated tips as used in this work (Su *et al. Nanoscale*, 2016, **8,** 10564–10569). As discussed in Supplementary Note 2, The high spatial resolution obtained in the TEPL map shown in Fig. S5b results from the enhancement of local electric field at the apex of Ag-coated tip due to LSP resonance with the 532 nm laser (A. Hartschuh *Angew. Chem. Int. Ed.* 2008, **47**, 8178-8191). The spatial resolution of a TEOS (TERS or TEPL) map has been previously shown to be similar to the radius of the metallic tip-apex (Xu *et al. J. Raman Spectrosc.* 2009, 40, 1343–1348; Petttinger *et al. J. Raman Spectrosc.* 2005; 36: 541–550; Behr *et al. J. Phys. Chem. C* 2008, 112, 3766-3773). The estimated spatial resolution of < 20 nm in the TEPL is consistent with the tip radius of ≈ 25 nm measured from the SEM image of a representative Ag-coated tip shown in the inset of Fig 1. Furthermore, this optical resolution is also similar to the TERS spatial resolution reported by our group on other samples such as single-layer graphene (Spatial resolution 16 nm: Su *et al. Journal of Vacuum Science & Technology B* 2013, 31(4), 041808; (Spatial resolution 20 nm: Su *et al.*Chem. Commun. 2016, 52, 8227; Spatial resolution 24 nm: Mignuzzi *et al. Nanoscale* 2015, 9, 19413) and map of a photocatalytic reaction on silver catalysts (Spatial resolution 20 nm: Kumar *et al. Nanoscale* 2015, 7, 7133–7137). The Ag-coated probes used in these reports were prepared following exactly the same procedure as used in this work.

Using the same fitting procedure the spatial resolution of the photocurrent map is estimated to be ≈ 15 nm in Fig S5d.

Supplementary Note 4

Probe depths of tip-enhanced Raman spectroscopy (TERS) and tip-enhanced photoluminescence (TEPL) signals

The probe depths of TER and TEPL signals can be determined by their dependence on the electric near-field intensity (E). In the near-field, intensity of Raman signals is $\propto E^4$, whereas the intensity of PL signals is $\propto E^2\eta$, where η is the PL quantum yield in the near-field, which can be different from the far-field (A. Hartschuh *Angew. Chem. Int. Ed.* 2008, **47**, 8178-8191). Due to the interaction of LSP of the metallic tip with the excitation laser, intensity of both Raman and PL signals is amplified as $\propto E^2$. For sufficiently small Raman shifts, the tip also enhances the Raman emission signals with the same factor ($\propto E^2$) leading to an overall E^4 proportionality for the Raman signals in the near-field. However, in the case of PL, the difference of the emission and excitation wavelengths are much larger compared to Raman. For example, at 532 nm excitation wavelength, the wavelength of Raman scattered photons corresponding to the 1382 cm^{-1} C8SiIDT-BT Raman band is 574 nm, whereas the wavelength of C8SiIDT-BT PL emission is 667 nm. Due to the finite energetic width of the LSP, the amplification of PL quantum yield η in the near-field is much weaker than the plasmonic enhancement of the Raman signals as shown below.

PL quantum yield of highly emissive samples in the far-field (η_0) is ≈ 1 and therefore cannot be enhanced further since it cannot be greater than 1. On the other hand, PL quantum yield of materials with low η_0 can be increased by several orders of magnitude in the near-field. Herein, we estimate the near-field enhancement in PL quantum yield for the polymer:fullerene blend sample used in this study using the EFs calculated in Supplementary Note 2 above. For Raman signals, $EF_{Raman} \approx (E/E_0)^4$, where EF_{Raman} is the EF of near-field Raman signals and E_0 and E are the intensities of electric field in the far-field and the near-field, respectively. For PL signals, $EF_{PL} \approx (E/E_0)^2 (\eta/\eta_0)$, where EF_{PL} is the EF of near-field PL signals (A. Hartschuh *Angew. Chem. Int. Ed.* 2008, **47**, 8178-8191). This can be rewritten as $EF_{PL} \approx (EF_{Raman})^{1/2} (\eta/\eta_0)$. Using the EF values ($EF_{PL}$ = 263 and EF_{Raman} = 851) for C8SiIDT-BT polymer calculated in the Supplementary Note 2 above we estimate an enhancement of η by only a modest factor of 9. This supports our assumption that the wavelength dependence of the plasmonic enhancement leads to a much lower amplification of PL signals in the near-field as compared to the Raman signals.

Since the enhancement of PL and Raman signals depends differently on the near-field intensity, their probe depths within the sample are different. We define probe depth of each signal as the depth at which the measured signal drops to 1/e relative to the signal at the sample surface. As the Raman signal enhancement decays much faster as a function of the near-field within the sample surface, TER signals are expected to have a shorter probe depth compared to the TEPL signals.

Supplementary Note 5

Further Details of Numerical Simulations

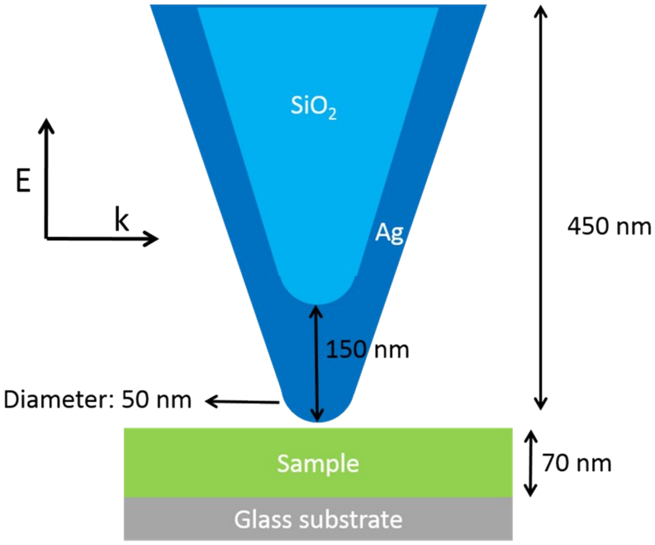

Fig. S8. Schematic diagram of the model used for numerical simulations to calculate electric field enhancement at the apex of Ag-coated tip and decay length of field enhancement within pristine polymer and fullerene films.

For electromagnetic (EM) numerical simulations, conical SiO_2/Ag tips with round apex were used in the geometric model set up in Comsol Multiphysics®, a commercial finite-element method solver used to solve Maxwell's equations. In the geometric model, the tip and sample characteristics were kept exactly same as the ones used experimentally in this work. For the Ag-coated tip, the height and angle were set to 450 nm and 45°, respectively. The nominal thickness of silver layer on SiO_2 tip was set to 150 nm along with the apex diameter of 50 nm. The thickness of polymer and fullerene films was set to 70 nm. Since all experimental measurements were performed in contact mode AFM, the distance between the Ag-coated tip and the sample was kept as 0.5 nm. A schematic diagram of the model is shown in Fig. S8. The optical constants of SiO_2 and Ag were taken from the reference, E. Palik, ed., *Handbook of optical constants of solids*, Academic Press, London, 1985, while the optical constants of fullerene and polymer were calculated using ellipsomteric measurements. The optical constants of different materials used in the model are listed in Table S4.

Table S4. Optical constants of the materials used in the model for numerical simulations.

Materials	**n**	**k**
Polymer	1.25	0.70
Fullerene	2.03	0.15
Ag	0.13	3.30
SiO_2	1.45	0
Glass	1.50	0

Extremely fine physics-controlled mesh was used in numerical simulations, which yields a minimum mesh size of 0.2 nm between the tip-apex and the sample surface. In order to simplify the calculation, a plane EM wave with 532 nm wavelength was used in this study, which is incident on the Ag-coated tip from the left side, with electric field parallel to the tip-axis as shown in Fig. S8. This configuration mimics the electric field with a radially polarised light, in which the most of the electric field in the laser spot is aligned parallel to the tip-axis.

Supplementary Note 6

Correlation of TEPL and photocurrent maps

An inverse correlation is expected between the polymer TEPL map shown in Fig. 3d and the photocurrent map in Fig. 3e. This is because a photogenerated electron – hole pair (exciton) within a polymer molecule can either recombine to emit a photon, which is measured as the polymer PL, or the photogenerated electron can be captured by a nearby fullerene molecule and collected by the Ag-coated tip, which is measured as the photocurrent. Therefore, the local polymer TEPL and photocurrent should be inversely correlated. This is shown in Fig. 3f where the average intensity of the polymer TEPL map and the photocurrent map over the topographic island region marked by the dashed rectangles in Fig. 3d and 3e (going from right to left) is plotted on the same graph. The polymer TEPL intensity is indeed found to be inversely correlated to photocurrent.

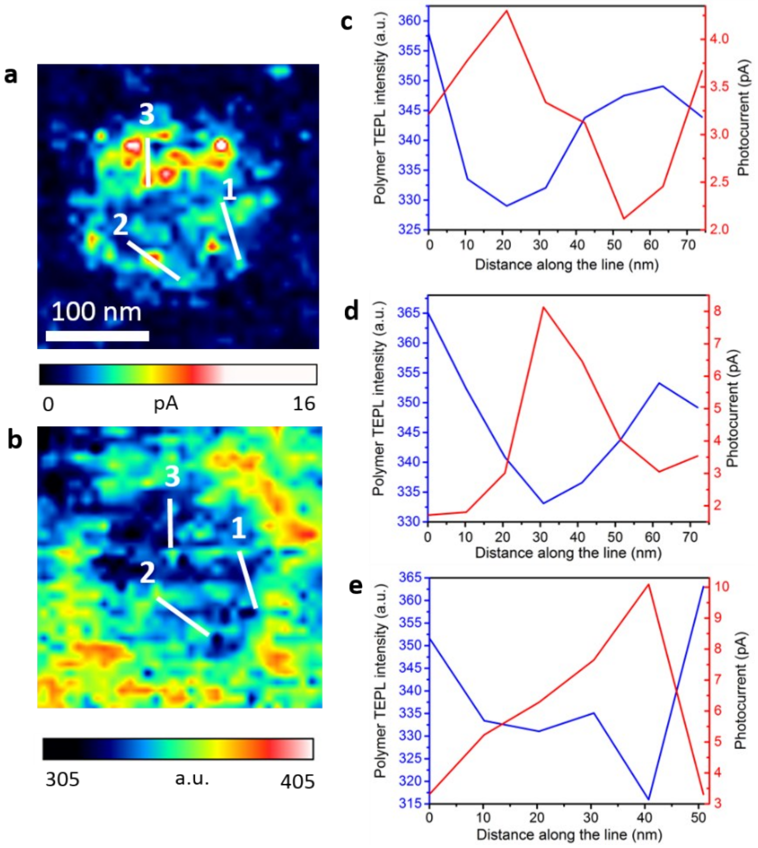

Fig. S9. Zoomed-in areas of (a) photocurrent map shown in Fig. 3e and (b) polymer TEPL map shown in Fig. 3d. (c) – (e) Correlated intensity profiles along lines marked as 1, 2 and 3, respectively in Fig. S9a and S9b. TEPL intensity is plotted in blue and the photocurrent intensity is plotted in red.

Herein, we present further analysis of correlated intensity profiles in different areas of polymer TEPL and photocurrent maps in Fig. 3d and 3e. Fig. S9a and S9b show zoomed in areas of the photocurrent map shown in Fig. 3e and the polymer TEPL map shown in Fig. 3d. Correlated line profiles along lines 1, 2 and 3 marked in Fig. S9a and S9b in different regions of the maps are plotted in Fig. S9c – S9e. The polymer TEPL and the photocurrent intensities are indeed found to be inversely correlated along all three line profiles. It should be noted that the pixel size in these line profiles is 10 nm.

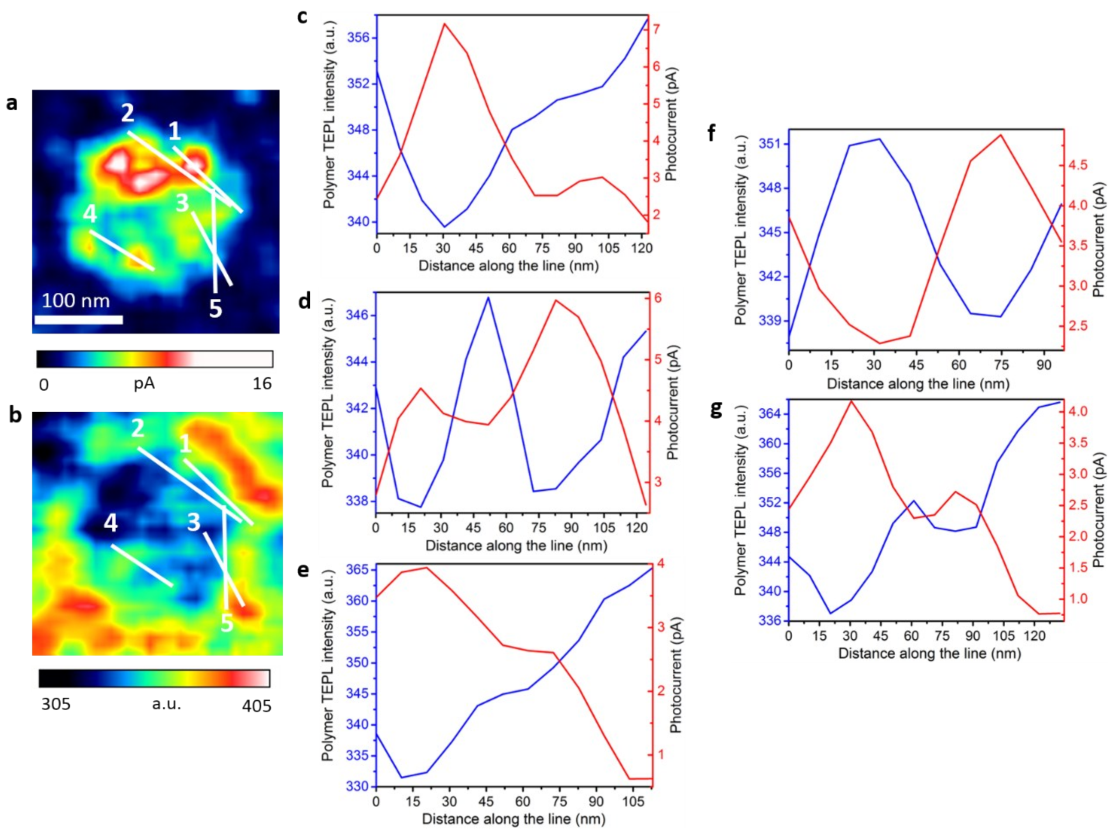

Fig. S10. Zoomed-in and smoothened (mask size: 3x3) maps of (a) photocurrent map shown in Fig. S9a and (b) polymer TEPL map shown in Fig. S9b. (c) – (g) Correlated intensity profiles along the line 1 - 5, respectively marked in Fig. S10a and S10b. TEPL intensity is plotted in blue and the photocurrent intensity is plotted in red.

Fig. S10a and S10b show the smoothened polymer TEPL and photocurrent maps shown in Fig. S9a and S9b, respectively. Smoothening is performed by applying a mask of 3x3 pixels such that the intensity of every pixel in Fig. S10a and S10b is equal to the average intensity of 3x3 pixels around the corresponding pixel in Fig. S9a and S9b. Fig. S10c – S10g show the correlated polymer TEPL (blue colour) and photocurrent (red colour) intensity profiles along lines 1 – 5, respectively marked in Fig. S10a and S10b. Once again, an inverse correlation of the polymer TEPL and photocurrent intensity is observed in all line profiles from different parts of the maps in Fig. S10a and S10b. This indicates that the data in the nanoscale TEPL maps is indeed reliable and correlates very well with the corresponding data in the photocurrent map at the nanometre length-scales. Furthermore, this also indicates that the variation of intensities in the TEPL map is not caused by random fluctuations but arise due to the interplay of nanoscale excitonic processes at the polymer – fullerene interfaces.

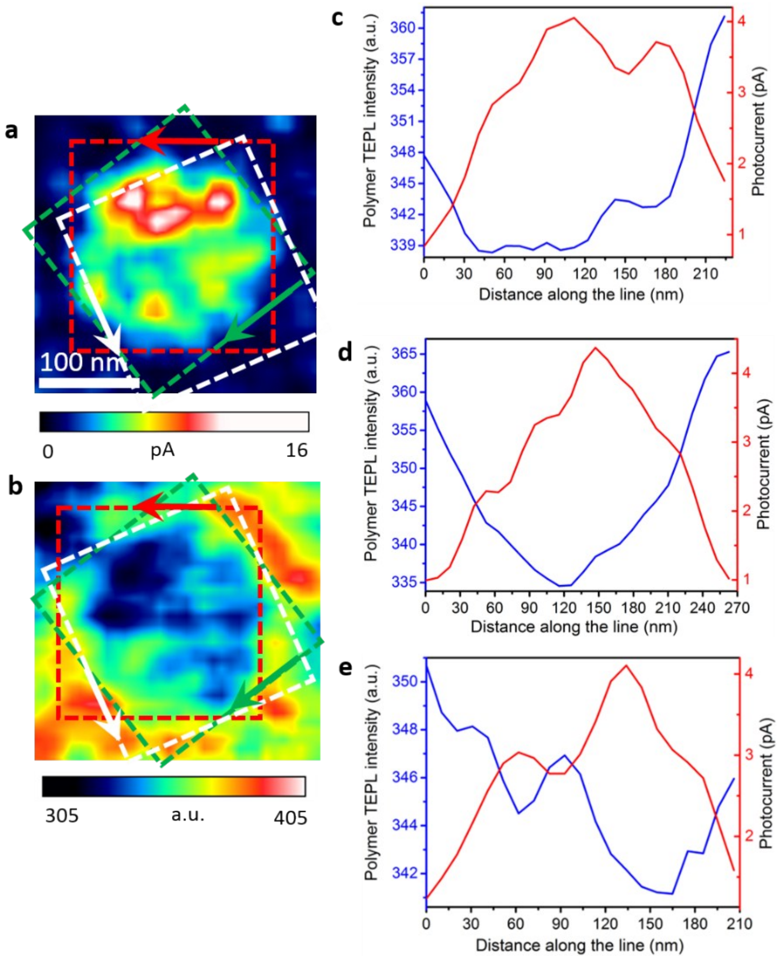

Fig. S11. Zoomed-in and smoothened maps of (a) photocurrent map shown in Fig. S9a and (b) polymer TEPL map shown in Fig. S9b. (c) – (e) Correlated average intensity profiles over the entire island region marked by dashed red, white and green squares, respectively in Fig. S11a and S11b. The direction of intensity averaging is indicated by arrows along one side of the squares. TEPL intensity is plotted in blue and the photocurrent intensity is plotted in red.

Lastly, we plotted the correlated average intensity over the entire island region in the polymer TEPL and photocurrent maps shown in Fig. S11a and Fig. S11b. Average intensity profiles over the regions marked by dashed red, white and green squares in Fig. S11a and S11b are plotted in Fig. S11c – S11e, respectively. The direction of intensity averaging is indicated by the arrows marked along one side of the squares. It can be clearly seen that the even along different direction in the island region the polymer TEPL intensity show a perfectly inverse correlation with the photocurrent intensity, which further corroborates the validity of the high spatial resolution obtained in the TEPL map.

Supplementary Note 7

Simultaneous topography, electrical and optical microscopy of pristine and annealed operating C8SiIDT-BT:PC$_{61}$BM solar cell devices

We carried out STEOM measurements of C8SiIDT-BT:PC$_{61}$BM (1:1) solar cell devices before and after thermal annealing, using the same experimental set-up as shown in Fig. 1 and S1. In contrast to the C8SiIDT-BT:ICMA blend topography that consists of islands with diameter ranging from 50 – 250 nm as shown in Fig. 2b, topography of C8SiIDT-BT:PC$_{61}$BM blend shown in Fig. S12a shows absence of any large-scale (sub-micron) features indicating a more intimate mixing of the C8SiIDT-BT & PC$_{61}$BM molecules. Fig. S12b – S12f show high-resolution maps of topography, PC$_{61}$BM 4693 cm^{-1} PL band intensity, C8SiIDT-BT 1382 cm^{-1} Raman band intensity, C8SiIDT-BT 3800 cm^{-1} PL band intensity and photocurrent measured simultaneously from 1 × 0.5 µm^2 area (marked with the dotted rectangle in Fig. S12a) of the C8SiIDT-BT:PC$_{61}$BM solar cell device. Topography map in Fig. S12b confirms absence of any large size features on the blend surface. TEOS maps of PC$_{61}$BM PL intensity, C8SiIDT-BT Raman intensity and C8SiIDT-BT PL band intensity in Fig. S12c – S12e indicate a uniform distribution of polymer and PC$_{61}$BM molecules in the blend film and absence of any phase-separated domains formed by the aggregation of the polymer or fullerene molecules at the surface or subsurface.

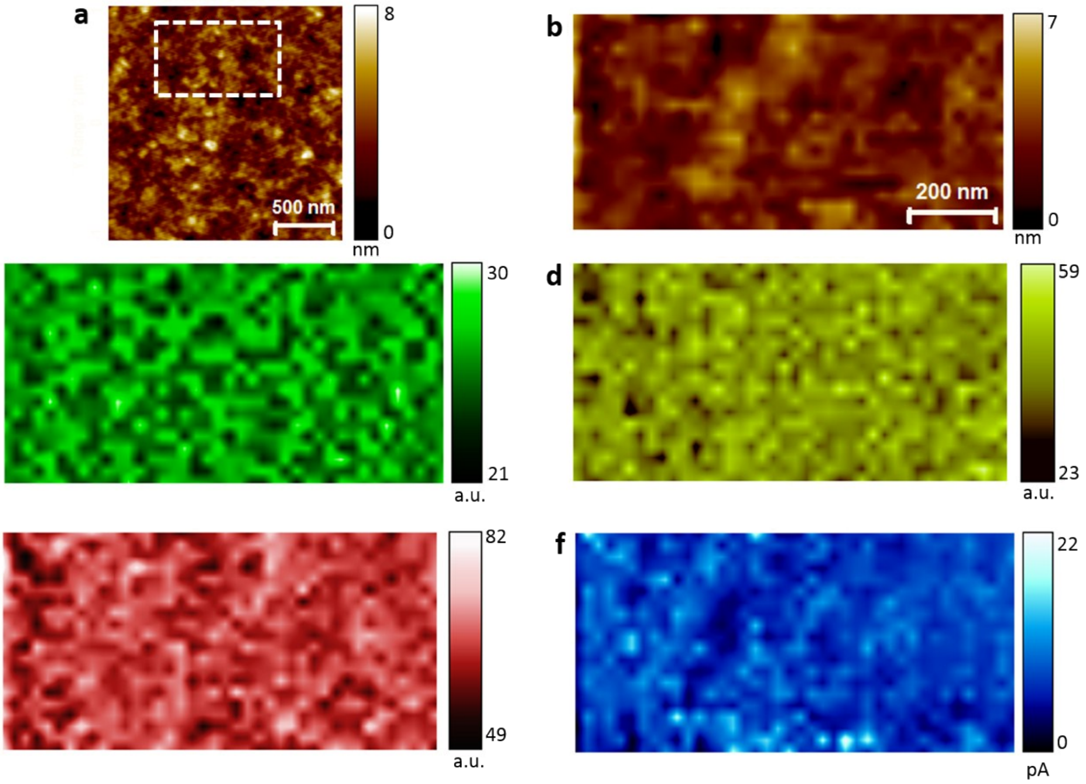

Fig. S12. (a) AFM topography image of C8SiIDT-BT:PC$_{61}$BM blend surface. High resolution maps of (b) topography (c) PC$_{61}$BM 4693 cm^{-1} (709 nm) PL band intensity (d) C8SiIDT-BT 1382 cm^{-1} Raman band intensity (e) C8SiIDT-BT 3800 cm^{-1} (667 nm) PL band intensity and (f) photocurrent measured simultaneously from 1.0 × 0.5 µm^2 area of operating C8SiIDT-BT:PC$_{61}$BM solar cell device with 40 × 20 pixels. Spectrum integration time: 0.5 s.

Furthermore, compared to the C8SiIDT-BT:ICMA blend solar cell device, a relatively more uniform generation of photocurrent from the C8SiIDT-BT:PC$_{61}$BM blend surface is observed in Fig. S12f, consistent with a mixed C8SiIDT-BT:PC$_{61}$BM phase in the blend. This is consistent with the macroscopic performance of pristine C8SiIDT-BT:PC$_{61}$BM and C8SiIDT-BT:ICMA solar cells as listed in Supplementary Table S1, where the measured photocurrent is more than twice as high for the PC$_{61}$BM blend while the open circuit voltage and the fill factor of both solar cells are very similar.

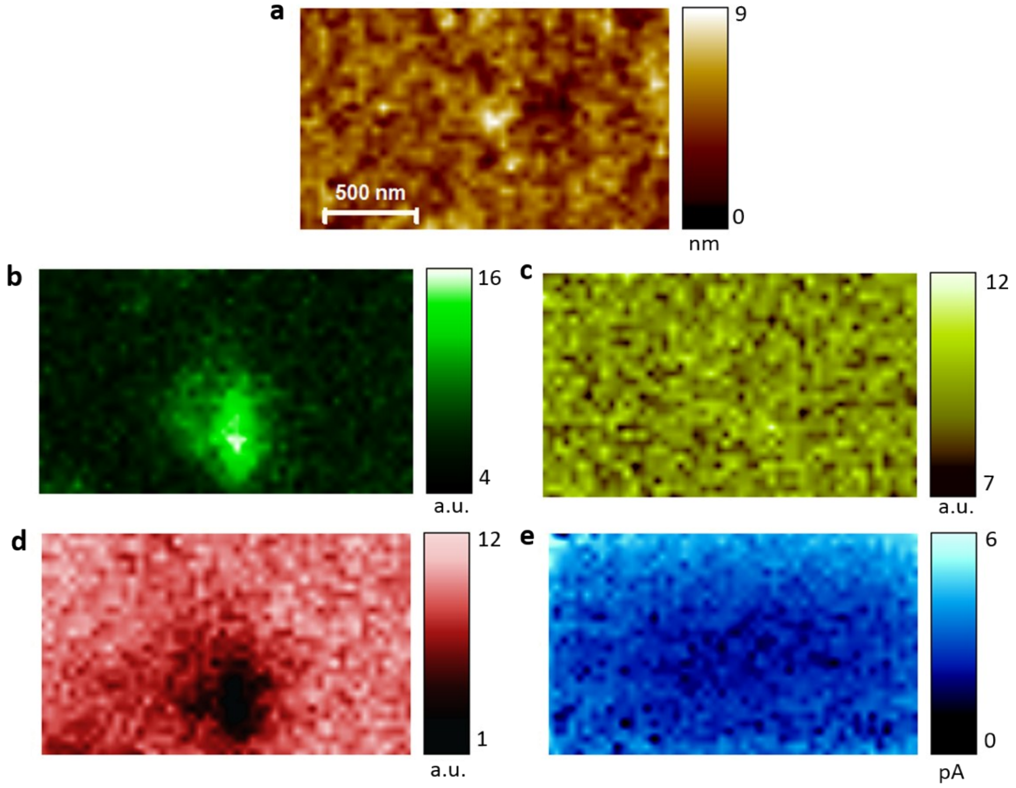

Fig. S13. High-resolution maps of (a) Topography, (b) PC$_{61}$BM 4693 cm^{-1} (709 nm) PL band intensity, (c) C8SiIDT-BT 1382 cm^{-1} Raman band intensity, (d) C8SiIDT-BT 3800 cm^{-1} (667 nm) PL band intensity and (e) photocurrent from 2.0 × 1.2 µm^2 area of annealed C8SiIDT-BT:PC$_{61}$BM solar cell with 50 × 30 pixels. Spectra integration time: 0.5 s.

Finally, we performed STEOM measurements of C8SiIDT-BT:PC$_{61}$BM (1:1) solar cell device thermally annealed at 150° for 30 minutes. The high resolution maps of topography, PC$_{61}$BM PL band intensity, C8SiIDT-BT Raman band intensity, C8SiIDT-BT PL band intensity and photocurrent measured simultaneously from 2 × 1.2 µm^2 area are shown in Fig. S13a – S13e. The topography image shows absence of any large scale features on the surface. However, the PC$_{61}$BM PL intensity map in Fig. S7b shows that a fullerene rich domain is formed after thermal annealing presumably at the sub-surface. Furthermore, the C8SiIDT-BT Raman and PL intensity maps in Fig. S13c and S13d and the photocurrent map in Fig. S13e indicate that this fullerene domain is relatively pure in composition as the polymer PL decreases without any corresponding increase in the photocurrent, unlike the case of C8SiIDT-BT:ICMA blend solar cell in Fig. 3, where a high photocurrent is observed at such locations due to a nanoscale distribution of polymer molecules around the fullerene aggregates. This result clearly indicates a difference in the ability of ICMA and PC$_{61}$BM to mix with this indacenodithiophene (IDT) polymer. Furthermore, thermal annealing leads to an overall reduction in photocurrent generation efficiency (lower photocurrent) of the device. In fact, the average photocurrent per pixel falls from 7.1 pA in Fig. S12f for the pristine C8SiIDT-BT: $PC_{61}BM$ solar cell to 4.0 pA in Fig. S13e for the annealed C8SiIDT-BT: $PC_{61}BM$ solar cell showing a 44% reduction upon thermal annealing. This result is also remarkably consistent with the macroscopic performance of pristine and annealed C8SiIDT-BT: $PC_{61}BM$ solar cell listed in Supplementary Table S3, which show a significant reduction in device performance with a decrease of both photocurrent and PCE by 50% and 64% upon thermal annealing.

These results demonstrate the potential of STEOM measurements to explain the macroscopic performance of OPV devices in terms of their morphological, chemical and photoelectrical characteristics at the nanoscale.

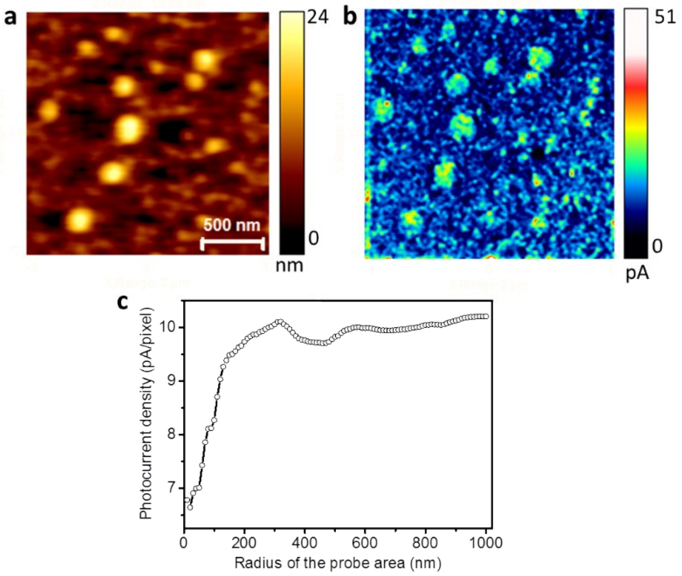

Fig. S14. (a) AFM topography image of a 2 × 2 µm^2 area of the C8SiIDT-BT:ICMA (1:1) solar cell. (b) Photocurrent map of the blend area in S14a measured under short circuit conditions, showing high photocurrent at the location of topographic islands. (c) Average photocurrent per pixel (calculated in a circular region) as a function of the radius of circular area. Circular area was calculated using the radius of a circle centered in middle of Fig. S14b, and truncated when it became large enough to reach the end of the image. Radius step size: 10 nm. All pixels covered (even partially) by the circle were included in the calculation. It should be noted that the photocurrent response becomes apparently homogeneous when the radius of the circular area approaches 1 µm.

Supplementary Note 8

Far-field optical mapping

Fig. S15 shows the far-field measurements of the 500 × 500 nm^2 sample area marked by dashed square in Fig. S15a. The far-field maps of the intensity of fullerene photoluminescence (PL) signal, polymer Raman signal and polymer PL signal are shown in Fig. S15b – S15d, respectively. It can be clearly seen that unlike TEPL images no variation in the intensity of any of these signals can be observed in the far-field maps. Furthermore, no correlation can be obtained with the corresponding topographic features in Fig. S15a. Fig. S15e shows two far-field spectra measured at position marked as 1 and 2 in Fig. S15a. Fig. S15f shows these two far-field spectra vertically shifted. It can be observed in Fig. S15e and S15f that no discernible difference can be found in the PL or Raman intensity at the two locations, which confirms that the lower sensitivity and lower lateral and axial resolution of far-field measurements are not enough to obtain information about molecular distribution in these samples at the nanometre length-scales.

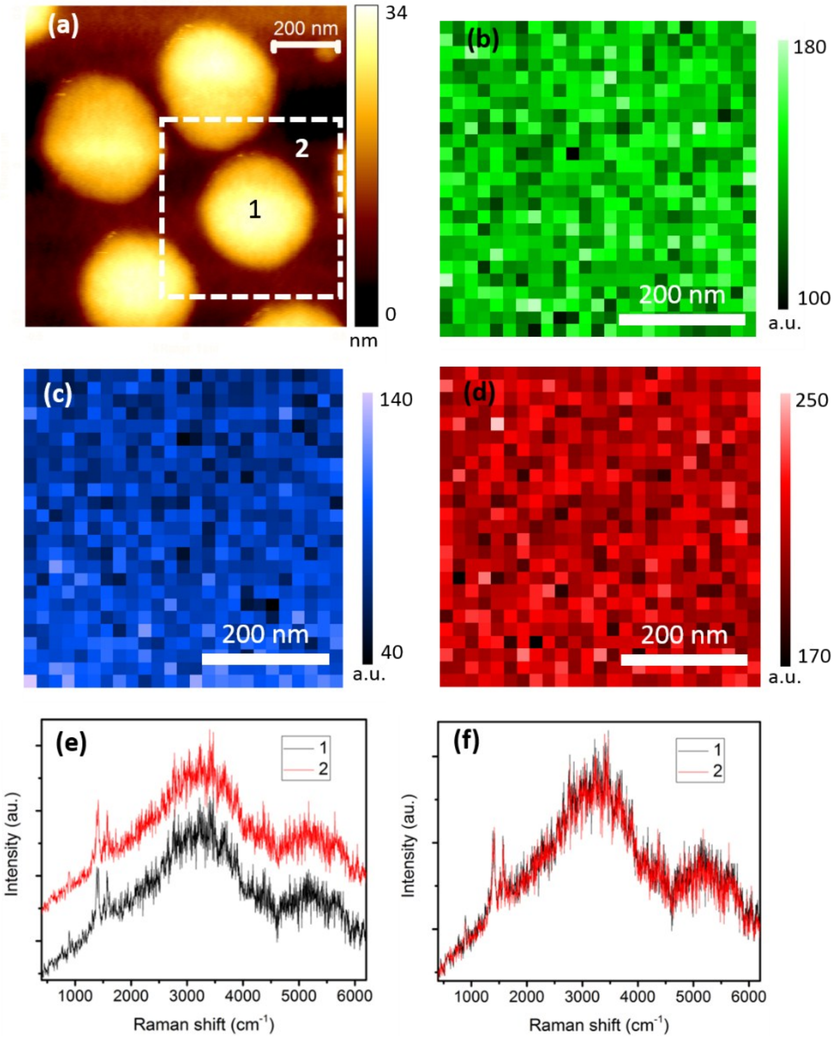

Fig. S15. (a) AFM topography image of 1×1 μm^2 area of the C8SiIDT-BT:ICMA (1:1) blend used as solar-cell active layer in this work. Far-field maps (25 × 25 pixels) of the intensity of (b) fullerene PL signal (5400 cm^{-1}), (c) polymer Raman signal (1382 cm^{-1}) and (d) polymer PL signal (3800 cm^{-1}) measured in the 500 × 500 nm^2 region marked by a dashed square in S15a. (e) Far-field spectra measured at positions 1 and 2 marked in S15a. (f) Far-field spectra shown in S15e, vertically shifted to show the difference in Raman and PL intensities. Spectrum integration time: 0.5 s.